New investigation of the ν 3 C-H stretching region of 12CH4 through the analysis of high temperature infrared emission spectra

B. Amyay, A. Gardez, Robert Georges, Ludovic Biennier, J. Vander Auwera, C. Richard, Vincent Boudon

New investigation of the ν_3 C-H stretching region of $^{12}CH_4$ through the analysis of high temperature infrared emission spectra

Badr AMYAY[a,*], Aline GARDEZ[b], Robert GEORGES[b], Ludovic BIENNIER[b], Jean VANDER AUWERA[c], Cyril RICHARD[a], Vincent BOUDON[a,*]

[a]*Laboratoire Interdisciplinaire Carnot de Bourgogne (ICB), UMR 6303 CNRS, Université Bourgogne Franche-Comté 9 avenue A. Savary, BP 47870, 21078 DIJON Cedex, France*
[b]*Institut de Physique de Rennes, UMR 6251, Campus de Beaulieu, Université de Rennes 1/CNRS, F-35042 Rennes Cedex, France*
[c]*Service de Chimie Quantique et Photophysique, C.P. 160/09, Université Libre de Bruxelles, 50 avenue F. D. Roosevelt, B-1050 Brussels, Belgium*

Abstract

The ν_3 C-H stretching region of methane was reinvestigated in this work using high temperature (620-1715 K) emission spectra recorded in Rennes under Doppler limited resolution. This work follows our recent global analysis of the Dyad system $\Delta n = \pm 1$ (1000 – 1500 cm^{-1}), n being the polyad number [B. Amyay *et al.* J. Chem. Phys., **144**, (2016), 24312]. Thanks to the high temperature, new assignments of vibration-rotation methane line positions have been achieved successfully in the Pentad system and some associated hot bands ($\Delta n = \pm 2$) observed in the spectral region 2600-3300 cm^{-1}. In particular, rotational assignments in the cold band (Pentad−GS) and in the first related hot band (Octad−Dyad) were extended up to $J = 30$ and 27, respectively. In addition, 1525 new transitions belonging to the Tetradecad−Pentad hot band system were assigned for the first time, up to $J = 20$. The effective global model used to deal with the new assignments was developed to the 6^{th} order for the first three polyads (Monad, Dyad and Pentad), and to the 5^{th} order for both the Octad and the Tetradecad. 1306 effective parameters were fitted with a dimensionless standard deviation σ = 2.64. The root mean square deviations d_{RMS} obtained are 4.18 $\times$ 10^{-3} cm^{-1} for the Pentad−GS cold band, 2.48 $\times$ 10^{-3} cm^{-1} for the Octad−Dyad, and 1.43 $\times$ 10^{-3} cm^{-1} for the Tetradecad−Pentad hot bands, respectively.

*Corresponding author

March 16, 2018

1. Introduction

Methane ($^{12}CH_4$) is the simplest and one of the most important organic compound. It is involved in many research domains from fundamental to applied sciences [1, 2, 3] and present in several astrophysical environnements. In the Earth's atmosphere, it contributes from 4 to 9 $\%$ to the greenhouse effect with a relatively high lifetime of 8-10 years [4]. About 50$\%$ of methane global emissions are produced by human activities such as mining industry, farming and ranching [5]. Methane is a major constituent of the atmospheres of the giant planets such as Jupiter [6, 7], Saturn [8], Uranus [9], Neptune [10] and their main satellites such as Titan [11] and Triton [12], and the dwarf planet Pluto [13, 14]. It is also produced in the circumstellar envelopes of hot carbon stars, such as IRC+10216 with a relative abundance to H_2 of 3.5 $\times$ 10^{-6} [15], and in ultra-cool carbon stars of type T $\&$ Y-brown dwarfs [16, 17, 18] where it is believed to play an important role in processes leading to the formation of complex organic molecules [19]. Furthermore, methane is considered to be a signature of biological activity and hence is used to probe the potentially habitable extrasolar planets. It has already been detected in the atmosphere of some giant hot-Jupiter type exoplanets [20, 21, 22] and was shown to dominate the opacity of HD 189733b extrasolar planet in the 3 μm infrared spectral window [23].

Insert Figure 1

The vibrational energy levels involved in the 3 μm region (2600-3300 cm^{-1}), commonly known as the Pentad of methane, are illustrated in Figure 5. Since the 80's, several studies were devoted to the analysis of both line positions and line intensities in this region (see refs. [24, 25, 26, 27, 28, 29] and references therein). In particular, Hilico *et al.* [27] modeled the Pentad system with high accuracy (about 10^{-3} cm^{-1}) using a partly reduced fourth-order Hamiltonian for line positions. Most of these works focus on the study of the Pentad interacting states separately from the other polyads (local approach). A global approach was then adopted by S. Albert *et al.* [30] and refined by Daumont *et al.* [31] for both line positions and line intensities of all polyads up to the Octad system from 0 to 4800 cm^{-1}. In this model, the effective Hamiltonian was developed to the 6^{th} order for the two lowest polyads and to the 5^{th} order for the Pentad and Octad polyads. This analysis was then extended by Nikitin *et al.* [32] to achieve the first detailed analysis in the Tetradecad band system. In these successive studies, the experimental data used were essentially coming from high resolution infrared and Raman spectra at low and room temperature and therefore rotationally limited to $J = 20$. As a result, such models are adequate to predict spectra at low or moderate temperature for atmospheric and planetary applications. However, they are unable to reproduce high temperature spectra, which are essential to model accurately the opacities of hot astrophysical objects such as brown dwarfs and extrasolar planets, the temperatures of which can exceed by far 1500 K.

The emergence of new experimental techniques such as the High Enthalpy Source (HES), developed by R. Georges and coworkers, coupled to a high-resolution Fourier transform spectrometer (FTS) allows the recording of high temperature emission spectra of polyatomic molecules (C_2H_2 and CH_4) [33, 34, 35] up to about 2000 K. Recently, a new experimental setup coupling the HES

to a cw-cavity ring-down spectrometer has been developed by the same group to investigate rotationally cold hot bands of polyatomic molecules in the 1.5-1.7 μm region [36]. Hargreaves *et al.* developed an original approach to produce emission-corrected FTIR transmittance spectra of hot gases such as methane [37] and ethane [38]. Such high temperature spectra are of great relevance because they bring considerable information on high J-transitions - up to $J = 30$ - and hot bands originating from highly excited polyads. These latter bands are essential for high temperature opacity calculations.

Infrared databases of methane have been recently updated with information derived from the analysis of high temperature emission spectra of the Dyad system around 1400 cm^{-1} [35]. Indeed, 14415 vibration-rotation transitions belonging to the cold band and to three hot bands up to the Tetradecad were assigned, allowing significant improvements of the global effective model of methane to be achieved. These new spectroscopic data have been used for updating the MeCaSDa database [39], available online through our webpage [40], the Virtual Atomic and Molecular Data Centre (VAMDC) [41, 42] portal [43] and the HITRAN database [44]. However, a complete review of the modifications and new additions to our calculated spectroscopic relational databases will be the subject of a forthcoming paper.

Before extending the global model to the treatment of highly excited polyads beyond the Tetradecad ($>$ 6000 cm^{-1}), our database needs to be complemented with high-J transitions. Our methodology is to perform successive global analyses in the main five different spectral regions (Monad, Dyad, Pentad, Octad and Tetradecad) of methane. This was recently done in the Dyad region [35] and extended to the Pentad system in the present work.

The experimental setup used to record hot emission spectra is presented in section 2. Section 3 gives an overview of the theoretical model used for building the effective Hamiltonian and describes the concept of vibration-rotation polyads in detail. Then, in section 4, the global analysis of line positions and results are presented before concluding in section 5.

2. Experimental setup

2.1. Experiment

The gas sample was heated using a High Enthalpy Source, already described in details elsewhere [33]. Resistive heating of the porous graphite rod was achieved by the application of a high electric current (between 20 and 130 A in the present study). The 8-mm inner diameter hollow rod was supplied with a continuous flow of methane (1.5 to 3 l_n/min, i.e. normal liter per minute under normal conditions, P = 1 atm, T = 273 K), admixed with a small amount of carbon monoxide (0.1 l_n/min) used as a rotational thermometer to determine *a posteriori* the temperature of the gas. Flows of methane and carbon monoxide were precisely controlled with the use of MKS mass flow controllers. The initially cold incoming gas was heated by migrating radially through the high temperature porous walls of the hollow graphite rod. Continuous flowing conditions ensured a constant renewal of the sample in the furnace tube, which might be otherwise degraded by pyrolysis. The hot gas was evacuated through one end of the tube opening into a chamber maintained

at low pressure by a pumping unit. The infrared light emitted by the gas contained in the graphite furnace cavity was collected and focused by two toroidal mirrors onto the entrance port of a high resolution FTS (Bruker IFS 125 HR). The collecting mirrors housing and FTS were both maintained at low pressure to avoid any unwanted atmospheric absorption. A CaF_2 window was used to isolate the collecting mirror housing and the FTS from the vacuum chamber. A water-cooled foil of tantalum was used to shield the CaF_2 window from the hot gas ejected from the HES. A 2-mm aperture was drilled into the foil to allow infrared radiations to reach the collecting mirror while limiting the radiation produced by the graphite walls. A continuous counter flow of dry nitrogen was flushed in the space between the CaF_2 window and the foil of tantalum to prevent any methane penetration into this space, which would lead to an unwanted absorption of the infrared emission produces by the high-temperature gas.

Insert Table 1

The FTS was equipped with a CaF_2 beamsplitter and a liquid nitrogen cooled InSb detector. An appropriate band-pass filter, including both the Pentad region of methane and the 1–0 emission band of CO, was used to increase the signal-to-noise ratio (a low-pass filter was used to record the spectrum at 1404 K). According to the temperature, the instrumental resolution was either set to 0.008, 0.012 or 0.02 cm^{-1} to match the Doppler broadening of the lines. Taking advantage of the stability of the HES over time, several hundreds of scans could be co-added to increase the signal-to-noise ratio of the recorded spectra. For example, the recording time corresponding to 2000 scans at 0.02 cm^{-1} resolution is about 15h.

The most intense methane emission lines were compared with those listed in the HITRAN 2008 molecular spectroscopic database [45], characterized by uncertainties in the range 10^{-4}-10^{-2} cm^{-1}. A typical wavenumber shift of 10^{-3} cm^{-1} was found and no calibration was applied to the experimental emission spectra. In addition, there was no inter-calibration of the measured positions in the $P_1 - P_0$ and $P_2 - P_1$ (previous work [35]) and $P_2 - P_0$ (this work) bands.

2.2. Experimental data

Six emission spectra of methane were recorded under different experimental conditions (see Table 1). They are displayed in Figure 2. Temperatures were extracted from a Boltzmann plot of the relative intensities measured in the 1–0 $^{12}C^{16}O$ emission band. The uncertainty on these values results mainly from the self-absorption affecting the strongest emission lines.

Insert Figure 2

The quality of the recorded spectra is highlighted in Figure 3 in a small window between 3146 and 3158 cm^{-1}. As illustrated by this figure, the spectrum at 1404 K produced the most exploitable spectral data. Indeed, it exhibits the best signal to noise ratio and was recorded at a resolution (0.008 cm^{-1}) significantly higher than the Doppler width of methane lines (equal to 0.018 cm^{-1} at 2700 cm^{-1}). This is essential for the assignment procedure, in particular when

considering the contribution of the weakest lines originating from the hot bands. The other spectra were used all along the analysis for confirming assignments and comparisons.

The line positions were measured using the "WSpectra" program [46], considering a Gaussian line profile and including instrumental effects (i.e. the truncation of the interferogram and effects of the finite size of the entrance aperture of the spectrometer). As the spectra were rather dense, the precision of measurement of line positions was significantly affected by line blending. It was determined with the help of the previous global model predictions [35] and comparisons with line positions from the literature [30, 32]. We checked that the well known and strongest lines that are free of overlaps are reproduced within 0.001 cm^{-1} in the case of the cold band. The value of 0.005 cm^{-1} was considered for the first hot band (Octad−Dyad) and 0.008 cm^{-1} for the second hot band (Tetradecad−Pentad). One should mention that the precision of the line positions may drop to about 0.02 cm^{-1} for blended or weakest lines.

Insert Figure 3

3. Theory

3.1. The effective Hamiltonian

The theoretical background of effective vibration-rotation Hamiltonian of tetrahedral molecules is detailed in our previous work [35] and will be briefly recalled here. The notations used throughout this paper are defined in this section.

The conventional normal modes of methane ($^{12}CH_4$) are respectively: the ν_1 mode, a non-degenerate symmetric CH stretching vibration with symmetry A_1, the ν_2 mode, a doubly degenerate CH bending vibration with symmetry E and two triply degenerate modes with symmetry F_2, the ν_3 being a CH stretching vibration and the ν_4 mode corresponding to a CH bending vibration. Their corresponding frequencies, exhibit an approximate relation between stretching and bending modes ($\nu_1 \simeq \nu_3 \simeq 2\nu_2 \simeq 2\nu_4$) defining the so-called vibrational polyads [47, 48, 49, 50, 51, 52]. Each polyad (P_n), is characterized using the quantum number of polyad n such as:

$$n = 2\left(v_1 + v_3\right) + v_2 + v_4, \tag{1}$$

where $v_{i=1,2,3,and\ 4}$ are the vibrational quantum numbers associated to the normal modes of methane.

The polyads P_n are numbered with increasing energy starting with P_0 for the Ground State (GS) or Monad, P_1 for the Dyad, P_2 for the Pentad, *etc*.

The resulting effective Hamiltonian of a given polyad can be written in tensorial form as a linear combination of the vibration-rotation operators such as:

$$\widetilde{\mathcal{H}}_{\{P_k\}} = \sum_{\text{all indexes}} \widetilde{t}^{\Omega(K,n\Gamma)\Gamma_v\Gamma_{v'}}_{\{s\}\{s'\}} T^{\Omega(K,n\Gamma)\Gamma_v\Gamma_{v'}}_{\{s\}\{s'\}}. \tag{2}$$

The term $\widetilde{t}^{\Omega(K,n\Gamma)\Gamma_{\rm v}\Gamma_{\rm v'}}_{\{s\}\{s'\}}$ corresponds to the effective parameters to be determined by fitting experimental line positions and the $T^{\Omega(K,n\Gamma)\Gamma_{\rm v}\Gamma_{\rm v'}}_{\{s\}\{s'\}}$ are vibration-rotation operators defined as

$$T^{\Omega(K,n\Gamma)\Gamma_{\rm v}\Gamma_{\rm v'}}_{\{s\}\{s'\}} = \beta \left[{}^{\varepsilon}V^{\Gamma_{\rm v}\Gamma_{\rm v'}(\Gamma)}_{\{s\}\{s'\}} \otimes R^{\Omega(K,n\Gamma)} \right]^{(\rm A_1)}, \tag{3}$$

where β is a numerical factor equal to $\sqrt{3}\left(-\sqrt{3}/4\right)^{\Omega/2}$ if $(K, n\Gamma) = (0, 0\rm A_1)$, and equal to 1 otherwise. As shown in Eq. (3), the vibration-rotation operators $T^{\Omega(K,n\Gamma)\Gamma_{\rm v}\Gamma_{\rm v'}}_{\{s\}\{s'\}}$ are obtained by the totally symmetric coupling of a vibrational operator ${}^{\varepsilon}V^{\Gamma_{\rm v}\Gamma_{\rm v'}(\Gamma)}_{\{s\}\{s'\}}$ and rotational operator $R^{\Omega(K,n\Gamma)}$.

The coupling scheme used in the STDS software [53] is described in ref. [49]. The vibrational operator ${}^{\varepsilon}V^{\Gamma_{\rm v}\Gamma_{\rm v'}(\Gamma)}_{\{s\}\{s\}}$ is generated by recursive coupling of the creation (a^+) and annihilation (a) elementary operators for each normal mode. $\varepsilon = \pm 1$, is the parity under time reversal. Rotational operators $R^{\Omega(K,n\Gamma)}$ are also built recursively from successive couplings of the elementary tensor $R^{1(1)} = 2\mathbf{J}$ using the method of Moret-Bailly [54, 55] and Zhilinskiĭ [56]. They are symmetrized using the O(3) $\supset T_d$ orientation matrix defined in ref. [57] and [58]. Ω is the degree in J_α operators.

The order of each individual term in Eq. (3) is defined as:

$$\mathcal{O}_H = \Omega + \Omega_{\rm v} - 2. \tag{4}$$

where, Ω and $\Omega_{\rm v}$ are the order of rotational and vibrational operators respectively.

The present work being dedicated to the simultaneous analysis of cold and hot bands implying polyads P_0 to P_4 of $^{12}CH_4$, the following effective Hamiltonian was therefore used:

$$\begin{aligned} \widetilde{H}^{\langle \text{Tetradecad} \rangle} &= \widetilde{H}^{\langle P_4 \rangle}_{\{P_0\}} + \widetilde{H}^{\langle P_4 \rangle}_{\{P_1\}} + \widetilde{H}^{\langle P_4 \rangle}_{\{P_2\}} + \widetilde{H}^{\langle P_4 \rangle}_{\{P_3\}} + \widetilde{H}^{\langle P_4 \rangle}_{\{P_4\}} \\ &= \widetilde{H}^{\langle \text{Tetradecad} \rangle}_{\{\text{GS}\}} + \widetilde{H}^{\langle \text{Tetradecad} \rangle}_{\{\text{Dyad}\}} + \widetilde{H}^{\langle \text{Tetradecad} \rangle}_{\{\text{Pentad}\}} \\ &\quad + \widetilde{H}^{\langle \text{Tetradecad} \rangle}_{\{\text{Octad}\}} + \widetilde{H}^{\langle \text{Tetradecad} \rangle}_{\{\text{Tetradecad}\}}. \end{aligned} \tag{5}$$

The number of fitted and non-fitted parameters in each term of equation 5 is detailed in Table 2 according to the order of development.

Insert Table 2.

3.2. The effective dipole moment

The effective electric dipole moment operators are expanded using the same principles as discussed above for energy levels. The laboratory-fixed frame (LFF) components ($\Theta = X, Y$ and Z) of the effective dipole moment μ are expressed as [49, 50]:

$$\widetilde{\mu}^{(A_2)}_{\Theta} = \sqrt{3} \sum_m \langle 1; m|\Theta\rangle \sum_{\{i\}} \sum_{\Gamma} \mu^{\{i\}} \left[C^{(1,F_1)} \otimes M^{(\{i\},F_2)} \right]^{(A_2)}. \tag{6}$$

The $\langle 1; m|\Theta\rangle$ are Stone coefficients [59], $C^{(1,F_1)}$ is the direction cosines tensor and $\{i\}$ denotes all the intermediate quantum numbers and symmetries. The $\mu^{\{i\}}$ are the parameters to be fitted using experimental intensity measurements. The untransformed and effective dipole moment operators are linked together through the same transformation that leads to the effective hamiltonian and this transformation is necessarily a sum of rovibrational operators [49]. Thus $\widetilde{\mu}$ is expanded in terms of vibration-rotation operators

$$M_{\gamma}^{(\{i\},F_2)} = \left(R^{\Omega(K,n\Gamma_r)} \otimes {}^{\varepsilon}V_{\{s\}\{s'\}}^{\Gamma_v\Gamma_{v'}(C_v)} \right)_{\gamma}^{(F_2)}, \tag{7}$$

where $\gamma = x, y, z$ are the molecule-fixed frame (MFF) components, with

$$\varepsilon = (-1)^{\Omega}. \tag{8}$$

In this case, the order of the development is defined as

$$\mathcal{O}_{\mu} = \Omega + \Omega_{\mathrm{v}} - 1. \tag{9}$$

Although this work is devoted to the global analysis of line positions it is important to mention that the dipole moment parameters in equation (6) should also be updated. This should be done according to the modifications of the effective Hamiltonian parameters. As a matter of fact, the eigenfunctions mixings, on which line intensity strongly depend, are improved each time a new global analysis is achieved.

4. Global Analysis

4.1. Line assignments

The Dijon assignment list of methane is based on several successive global analyses of methane spectra, in particular from the work of Albert *et al.* [30] up to the Octad and the work of Nikitin *et al.* [32] up to the Tetradecad. 19747 vibration-rotation transitions were published in this latter study. The assignment list includes data coming from different sources : infrared and Raman spectra of essentially the cold bands up to the Tetradecad and four hot bands : $(P_1 - P_1)$ and $(P_2 - P_2)$ in the far infrared region, and the $(P_2 - P_1)$ and $(P_3 - P_1)$ hot bands. A slightly different line list, including 4 additional lines (19751 transitions in total) belonging to the $(P_2 - P_0)$, was used as a benchmark for our previous global analysis in the Dyad region at high temperature [35].

The Dijon assignment list was then extended by including transitions published in the literature as follows:

- In the THz region (50 – 500 cm^{-1}), we included 193 data published by Boudon *et al.* [60]. They belong to the R branch of the $(P_0 - P_0)$ system and its related hot band $(P_1 - P_1)$. They cover rotational states up to J = 19 in the case of the cold band and J =14 for the hot band. They are reproduced, in the present work, within 0.143 $\times$ 10^{-3} cm^{-1} and 0.180 $\times$ 10^{-3} cm^{-1} respectively.

- In the Dyad region (1100 – 1500 cm^{-1}), we included 39 data published by Hilico *et al.* [61]. They concern the hot bands $(P_2 - P_1)$ and $(P_3 - P_2)$ systems. Furthermore, we included 413 data from the analysis of the spectrum published by Bronnikov *et al.* [62]. These data belong to the Dyad cold and hot bands systems up to the Tetradecad ($4\nu_4$-$3\nu_4$). The most important source of data in this region comes from our previous global analysis of high temperature emission spectra of methane [35]. Indeed, 14415 vibration-rotation transition resulted from this analysis. They concern the Dyad cold band and related hot bands of the type $\Delta n = \pm 1$ up to the Tetradecad.

Thus, the total number of transitions included is equal to 34811 in the analysis reported in ref. [35]. 1414 duplicate lines originating from different sources were removed from this assignment list, which was used for updating the MeCaSDa calculated database [39].

The resulting assignment list was then considered in the current study, which focuses on the Pentad system and in particular the region of the ν_3 C-H stretching band. This strong band was extensively studied in the literature and thus many data can be found. Before starting the analysis of the high temperature ν_3 emission spectra, we added 150 highly accurate transitions (3 kHz) from sub-Doppler resolution comb-referenced spectroscopy published by Abe *et al.* [63]. These data, even limited rotationally to $J = 14$, bring strong additional constraints to the effective model essentially in the Pentad interacting states. Other new highly-accurate measurements, performed by the Dunkerque group [64] and concerning the pure rotation lines, have also been included in our assignment list. Table 3 details the experimental information used in the analysis described in section 4.2, thus including line positions measured and assigned in the present work.

Insert Tab 3

As shown in Table 3, line positions belonging to the $(P_2 - P_0)$, $(P_3 - P_1)$ and $(P_4 - P_2)$ band systems were measured in this work. They were assigned using the the XTDS & SPVIEW software packages developed in Dijon [65]. Assignments are based on the systematic comparison of the predicted line positions of methane with the observed emission spectrum. According to the thermal population of involved polyads, only three vibration-rotation bands could be observed in the emission spectrum. The most intense one is the ν_3, cold band, which dominates the spectrum, followed by two related hot bands with relatively low intensity $(P_3 - P_1)$ and $(P_4 - P_2)$.

As a result of this analysis, the cold band assignment has been extended rotationally to $J = 30$ compared to $J = 22$ in the previous global analysis [35]. In addition, new transitions involving rotational states with $J \leq 22$ were also successfully assigned. Thus, 1309 line positions belonging to this band were assigned and included in our database. We then identified 3233 vibration-rotation transitions belonging to the Octad−Dyad system *i.e.* with $\Delta n = \pm 2$ using the same procedure. The calculated relative intensity of this hot band compared to the cold band is about 22 % without considering the self absorption effect. As the energy increases, the density of transitions grows rapidly making the assignments very complicated and spectral overlaps become the rule. This justifies the large number of assigned line positions for hot bands. As for the cold band, the range

of observed $J-$levels for this series of hot bands is significantly extended to $J = 27$. The same statement applies for the next weak hot band (Tetradecad−Pentad). 1525 new transitions belonging to this hot band were assigned up to $J = 20$.

The global effective Hamiltonian of the Pentad system has been extended from the 5^{th} to the the 6^{th} order, as for the lower polyads, to deal with the new assignments in the 3 μm region. Indeed, according to the complexity of vibration-rotation couplings in the Pentad system (Fermi and Coriolis interactions), discrepancies of more than 30×10^{-3} cm^{-1} were observed for some assigned lines belonging to the ν_3 cold band and the corresponding hot band $\nu_3 + \nu_4$. Most of theses lines are observed for the first time. They correspond to highly excited rotational states characterized by large $\alpha > 80$ quantum number. The extension to the 6^{th} order allowed the calculated line positions to be improved for the assigned lines. However, we also observed some local perturbations involving high J-states for which a satisfactory fitting could not be achieved. These lines were excluded from the global fit procedure to maintain the stability of the global model at this stage. A new investigation of the Octad and the Tetradecad is required in the near future.

Figure 4 compares previously assigned transitions in the Pentad system, including all vibrational levels from the literature, with those coming from the present analysis, focusing on the ν_3 vibrational state. The two types of data (Absorption/Emission) are complementary to each other. As shown in Figure 4, data coming from absorption spectra are limited rotationally to about $J = 20$ and $\alpha < 78$. However, at high temperatures, a set of other highly excited levels could be observed up to $J = 30$ and $\alpha = 106$, all belonging to the dominant vibrational state ν_3.

Insert Figure 4.

4.2. Results and discussion

Insert Figure 5

The Pentad polyad system is composed of 9 vibrational sub-states namely $\{[2\nu_2, (E, A_1)]; [\nu_3(F_2), \nu_1(A_1)]; [\nu_2 + \nu_4, (F_1, F_2)]; [2\nu_4, (E, A_1, F_2)]\}$. In this polyad, the bright state is the ν_3 vibrational state with a symmetry F_2. The interaction scheme between the Pentad sub-states is illustrated in Figure 5, up to the order 2 of the effective Hamiltonian development. The rotational dependence of the Pentad couplings is also highlighted using the order in (J_α) at the top of Figure 5. At the zero order, only two pure vibrational terms are present : the $\nu_k \longleftrightarrow \nu_k$ with (k=1 or 3) corresponding to the band centers of the infrared ν_3 band around 3018.529 cm^{-1} and Raman ν_1 band around 2932.369 cm^{-1}, respectively.

As shown in Figure 5, the other vibrational states are involved progressively in the interaction scheme by including the interactions with states characterized by the symmetries A_1 and F_2 at the first order, and A_2, E and F_1 symmetries at the second order of the development. The first rotational dependence in (J_α) is observed at the first order, which involves the $\nu_3 \longleftrightarrow \nu_3$ diagonal term. Considering the order of magnitude of the coupling terms, it can be shown that the most

important interactions are of the first order, which couple directly the ν_1 state with $2\nu_2$ and $2\nu_4$ states (Fermi-type interactions), followed by the interaction between ν_3 and $2\nu_4$ vibrational states. Thus, including the ν_1 Raman data is essential to determine directly the first order coupling terms [66], while the infrared data from the ν_3 C-H stretching band will contribute indirectly to the determination of these important couplings.

At the second order, the coupling mechanism becomes more complicated and one can see that the ν_3 vibrational state plays an important role, in particular in the case of small and local interactions. The couplings involving ν_3 in Figure 5 are highlighted using red arrows. The order of magnitude of such interactions is small compared to the other couplings. Furthermore, the rotational dependence of these couplings is such as $1 \leq \Omega \leq 2$, while most other couplings have no rotational dependency. Therefore, even if these interactions are small at low J values, they are significant at high J values. Such local perturbations are illustrated in the reduced energy plot (see Figure 1) and can be observed in Figure 9 for high J states.

Coriolis interactions are also relevant in the Pentad system. Taking advantage of our previous analysis in the Dyad, the $\zeta_{2,4}$ Coriolis type interaction, which occurs also in the Pentad between $2\nu_2$, $\nu_2 + \nu_4$ and $2\nu_4$, is well determined. Furthermore, the high order Coriolis type interaction, which couples directly the ν_1 state to the $\nu_2 + \nu_4$ state, is also taken into account. So, both direct and indirect interactions are required for achieving a consistent global fitting. However, only limited data up to $J = 17$ from the Raman active states are accessible compared to the infrared data which now reach $J = 30$-levels. Thus, to deal with the high J levels we expanded the Pentad effective parameters to the 6^{th} order compared to the previous analyses.

The global model resulting from our previous analysis of the Dyad emission spectrum [35] was considered as a starting model in this study. We firstly considered 1309 transitions from the cold band (P_2-P_0). The parameters of the Pentad system developed up to the 6^{th} order were fitted to the new observed data, while the other parameters were fixed to their initial values. This allowed updating the Pentad system parameters. We then used this model to fit progressively the observed data of hot bands. The effective parameters of the Octad and Tetradecad systems were thus fitted to the new transitions. Finally, 39614 transitions including 6067 newly assigned lines were fitted using 1306 effective parameters up to the Tetradecad.

The non-linear least-squares fit minimized the standard deviation:

$$\sigma = \sqrt{\frac{1}{N}\sum_{i=1}^{N}\left(\frac{\widetilde{\nu}_i^e - \widetilde{\nu}_i^c}{\Delta\widetilde{\nu}_i^e}\right)^2}, \tag{10}$$

where N is the total number of line positions, $\widetilde{\nu}_i^c$ are the calculated wavenumbers and $\Delta\widetilde{\nu}_i^e$ are the experimental uncertainties. Each experimental line positions $\widetilde{\nu}_i^e$ has the weight $1/(\Delta\widetilde{\nu}_i^e)^2$.

Fit residuals (Obs.- Calc.) for line positions corresponding to different bands are illustrated in Figure 6 and 7. For instance, in the cold band (Pentad-GS), 95 % of line positions are re-

produced within the spectral resolution $\pm 8 \times 10^{-3}$ cm^{-1} while 5% of the lines are reproduced within better than $\pm 15 \times 10^{-3}$ cm^{-1} on average. This latter value results from overlapped lines, excited rotational states (at the end of the R and P branches) and some local perturbations. The percentage decreases slightly in the case of hot bands according to the increase of the degree of overlap. In the case of the two hot bands (P_3-P_1) and (P_4-P_2), 72% and 50% respectively of observed lines are reproduced within $\pm 8 \times 10^{-3}$ cm^{-1}. The obtained standard deviations are respectively $\sigma_{Pentad-GS} = 4.18$ for the cold band, $\sigma_{Octad-Dyad} = 2.48$ for the first hot band and $\sigma_{Tetradecad-Pentad} = 1.43$ for the second hot band. The resulting global dimensionless standard deviation of the fit is equal to $\sigma = 2.69$.

We should stress here that the emission transitions assigned in the Dyad [35] and the Pentad region are less precise and exceed by far the number of absorption data assigned previously in [32]. Because of the rotational degeneracy in methane, which increases rapidly with J (see Figure 1), an observed line is the result of a mixture of several predicted transitions close to each other. For instance, about 50 % of observed lines in the cold band ($P_2 - P_0$) are a mixture of two or several predicted transitions of the same band (i.e. without considering hot bands). These blendings also contribute to increasing the residuals.

Insert Figure 6 and Figure 7.

As described in section 3.2, the effective dipole moment parameters were updated using the resulting global model of line positions together with intensity data observed at 296 K and published in refs [60, 30, 32]. Table 4 summarizes the number of fitted lines for each band as well as the fit statistics. The root mean square deviation d_{RMS} is defined as :

$$d_{RMS} = 100 \sqrt{\frac{1}{N} \sum_{i=1}^{N} \left(\frac{\mathrm{I_{obs}} - \mathrm{I_{calc}}}{\mathrm{I_{obs}}} \right)^2}, \tag{11}$$

where N is the number of observed data and the I_{obs} and I_{calc} are the experimental and calculated intensities at 296 K, respectively. Figure 8 displays the intensity fit results for the Pentad-GS cold band system, which is the subject of the present work. Fit results of the other bands are given as a supplementary material.

Insert Table 4 and Figure 8.

Figure 9 compares the observed spectrum at 1404 K with the spectrum calculated using the effective Hamiltonian resulted from this work. The emission line intensities are relative, calculated using optimal conditions, and include the self-absorption effect to be comparable with the observed spectrum. In order to highlight the contribution of the hot bands, we calculated each band separately. They are illustrated using different colors in the bottom of each sub-figure. For instance, the blue curve is used for the ($P_2 - P_0$), the green color is used for the ($P_3 - P_1$) and the cyan is used for the ($P_4 - P_2$) bands. The total contribution of the 3 bands is illustrated using the

grey color.

It is shown in Figure 9 that the cold band is dominating the spectrum opacity. Indeed, most of these transitions involve the ν_3 vibrational state which is the only bright state of the Pentad system. According to the order of magnitude of the coupling terms involving ν_3 (see Figure 5), a very small intensity borrowing to the other components is occurring. The contribution of the hot bands is also relevant in particular in the case of the Q branch (upper right sub-figure in Figure 9). The status of the current improvement is highlighted for the low (left) and the high (right) J range in the four lower sub-figures. At low J values, the Q, P and R branches are well reproduced even for the cold and hot bands. At high J values, most of the transitions are well reproduced while a few lines shows discrepancies typically smaller than 0.03 cm^{-1}. This can be due to the Coriolis interaction connecting the ν_1 to the $\nu_2 + \nu_4$ vibrational states. Since the Raman transitions included in our database are limited rotationally to J =17, this interaction is only indirectly determined from the ν_3 transitions.

Figure 9 also compares our calculated spectrum with the spectrum calculated using the Theoretical Reims-Tomsk Spectral data "TheoReTS" database based on the *ab initio* potential energy surface of methane [67]. As can be observed, the agreement for the line positions at low J values is quite good, in particular in the case of the Q branch. However, at high J values, large shifts (0.2 cm^{-1}) are observed in the case of TheoReTS line-list.

Insert Figure 9.

Low resolution 1 cm^{-1} infrared cross-sections of methane at 296 K are calculated and illustrated in Figure 10. In this figure, we give a global view of the current improvements for the six polyads involved in this analysis up to the Tetradecad (i.e. 6500 cm^{-1}). Three different databases are compared: MeCaSDa (red) [39], ExoMol (green) [68] and TheoReTS (blue) [67].

There is an overall good agreement with the ExoMol database cross-sections and quite larger differences with TheoReTS. But it should be emphasized that these two databases result from pure *ab initio* calculations, with no adjustable parameters, while our calculation result from the fit of experimental assigned lines. Thus, although our calculation may be less complete, it has a better accuracy, especially on line positions, for the transitions included in our global fit. It should also be mentioned that, to build Figure 10, we used the online 500 K TheoReTS line list, which has an intensity cutoff for low intensity line, leading to some "holes" in the cross-sections. The full TheoReTS database contains many more low-intensity lines.

Insert Figure 10.

5. Conclusion

In this work, we presented a new analysis of the ν_3 C-H stretching region of $^{12}CH_4$, relying on high temperature emission spectra recorded in Rennes between 620 and 1715 K. This work updates our previous global analysis achieved in the Dyad spectral region of methane (Δn = $\pm$

1) [35]. Thanks to the high temperature emission spectra of the Pentad system (Δn= $\pm$ 2), 6067 assignments of vibration-rotation line positions have been successfully achieved. In particular, the newly assigned lines extended the cold band rotationally up to J =30. Furthermore, two related hot bands have been observed, namely the Octad−Dyad and the Tetradecad−Pentad respectively, up to J = 27 and 20. Observed vibration-rotation lines were included in our analysis and fitted together with the existing lines using 1306 parameters with a dimensionless standard deviation of σ =2.64. The global effective model is extended in the case of the Pentad system to the 6^{th} order compared to the 5^{th} order in the previous work to deal with the new observations. Local perturbations were also identified at high-J values revealing the important role of the ν_1 Raman band in the Pentad system. Indeed, such problems are probably due to the Coriolis effect connecting the ν_1 state to the $\nu_2 + \nu_4$ states. The effective transition dipole moment parameters were also updated. The resulting MeCaSDa database of methane is available through its web page [40] and the VAMDC portal [41, 42]. In the near future, it will also be used to update the HITRAN [44] and GEISA [69] spectroscopic databases.

Acknowledgements

B.A., V.B. and C.R. thank the CNRS-ANR e-PYTHEAS project (contract ANR-16-CE31-0005-03) and the Université de Bourgogne – Franche Comté (UBFC) for financial support. J.V.A. acknowledges financial support from the "Fonds de la recherche scientifique F.R.S.-FNRS (Belgium, contract CDR J.0123.16). R.G. and L.B. acknowledge the Programme National "Plantologie" (PNP) and the Programme National "Physique Stellaire" (PNPS) of CNRS/INSU for their financial support.

Supplementary Material

- Supplementary Material (I) : Hamiltonian effective parameters for methane $^{12}CH_4$ up to the Tetradecad.
- Supplementary Material (II) : Assigned vibration-rotation transitions in the Pentad region of methane $^{12}CH_4$.
- Supplementary Material (III) : Fit residuals for line intensities of methane $^{12}CH_4$.

References

[1] Shemshad J, Aminossadati SM, Kizil MS. A review of developments in near infrared methane detection based on tunable diode laser. Sensors and Actuators B: Chemical 2012;171-172:77–92.

[2] Singh BK, Bardgett RD, Smith P, Reay DS. Microorganisms and climate change: terrestrial feedbacks and mitigation options. Nature Reviews Microbiology 2010;8:779–90.

[3] Getman RB, Bae YS, Wilmer CE, Snurr RQ. Review and Analysis of Molecular Simulations of Methane, Hydrogen, and Acetylene Storage in Metal–Organic Frameworks. Chemical Reviews 2012;112:703–23.

[4] Kirschke S, Bousquet P, Ciais P, Saunois M, Canadell JG, Dlugokencky EJ, et al. Three decades of global methane sources and sinks. Nature Geoscience 2013;6:813–23.

[5] Guzmán-Marmolejo A, Segura A. Methane in the Solar System. Boletín de la Sociedad Geológica Mexicana 2015;67:377–85.
[6] Irwin PGJ, Sihra K, Bowles N, Taylor FW, Calcutt SB. Methane absorption in the atmosphere of Jupiter from 1800 to 9500 cm^{-1} and implications for vertical cloud structure. Icarus 2005;176:255–71.
[7] Zhang X, Nixon CA, Shia RL, West RA, Irwin PGJ, Yelle RV, et al. Radiative forcing of the stratosphere of Jupiter, Part I: Atmospheric cooling rates from Voyager to Cassini. Planetary and Space Science 2013;88:3–25.
[8] Tran H, Flaud PM, Fouchet T, Gabard T, Hartmann JM. Model, software and database for line-mixing effects in the ν_3 and ν_4 bands of CH_4 and tests using laboratory and planetary measurements—II: H_2 (and He) broadening and the atmospheres of Jupiter and Saturn. Journal of Quantitative Spectroscopy and Radiative Transfer 2006;101:306–24.
[9] Sromovsky LA, Karkoschka E, Fry PM, Hammel HB, de Pater I, Rages K. Methane depletion in both polar regions of Uranus inferred from HST/STIS and Keck/NIRC2 observations. Icarus 2014;238:137–55.
[10] Karkoschka E, Tomasko MG. The haze and methane distributions on Neptune from HST–STIS spectroscopy. Icarus 2011;211:780–97.
[11] Hirtzig M, Bézard B, Lellouch E, Coustenis A, de Bergh C, Drossart P, et al. Titan's surface and atmosphere from Cassini/VIMS data with updated methane opacity. Icarus 2013;226:470–86.
[12] Lellouch E, de Bergh C, Sicardy B, Ferron S, Käufl HU. Detection of CO in Triton's atmosphere and the nature of surface-atmosphere interactions. Astronomy and Astrophysics 2010;512:L8.
[13] Young LA, Kammer JA, Steffl AJ, Gladstone GR, Summers ME, Strobel DF, et al. Structure and composition of pluto's atmosphere from the new horizons solar ultraviolet occultation. Icarus 2018;300:174–99.
[14] Lellouch E, Sicardy B, de Bergh C, Käufl HU, Kassi S, Campargue A. Pluto's lower atmosphere structure and methane abundance from high-resolution spectroscopy and stellar occultations. Astronomy and Astrophysics 2009;495:L17–21.
[15] Agúndez M, Fonfría JP, Cernicharo J, Kahane C, Daniel F, Guélin M. Molecular abundances in the inner layers of IRC +10216. Astronomy and Astrophysics 2012;543(A):48.
[16] Burgasser AJ, Geballe TR, Leggett SK, Kirkpatrick JD, Golimowski DA. A unified near-infrared spectral classification scheme for T dwarfs. The Astrophysical Journal 2006;637:1067–93.
[17] Cushing MC, Kirkpatrick JD, Gelino CR, Griffith RL, Skrutskie MF, Mainzer A, et al. The Discovery of Y Dwarfs using Data from the Wide-field Infrared Survey Explorer (WISE). The Astrophysical Journal 2011;743:50.
[18] Yurchenko SN, Tennyson J, Bailey J, Hollis MDJ, Tinetti G. The spectrum of hot methane in astronomical objects using a comprehensive computed line list. Proceedings of the National Academy of Sciences USA 2014;111:9379–83.
[19] Dartois E, Muñoz Caro MG, Deboffle D, Montagnac G, d'Hendecourt L. Ultraviolet photoproduction of ISM dust - Laboratory characterisation and astrophysical relevance. Astronomy and Astrophysics 2005;432:895–908.
[20] Swain MR, Tinetti G, Vasisht G, Deroo P, Griffith C, Bouwman J, et al. Water, Methane, and Carbon Dioxide present in the dayside spectrum of the exoplanet HD 209458b. The Astrophysical Journal 2009;704:1616–21.
[21] Tinetti G, Deroo P, Swain MR, Griffith CA, Vasisht G, Brown LR, et al. Probing the terminator region atmosphere of the Hot-Jupiter XO-1b with transmission spectroscopy. The Astrophysical Journal Letters 2010;712:L139–42.
[22] Barman TS, Konopacky QM, Macintosh B, Marois C. Simultaneous Detection of Water, Methane, and Carbon Monoxide in the Atmosphere of Exoplanet HR8799b. The Astrophysical Journal 2015;804:61.
[23] Swain MR, Vasisht G, Tinetti G. The presence of methane in the atmosphere of an extrasolar planet. Nature 2008;452:329–31.
[24] Brown LR, Toth RA, Robiette AG, Lolck JE, Hunt RH, Brault JW. Analysis of the ν_1 and ν_2+ν_4 bands of $^{12}CH_4$. Journal Molecular Spectroscopy 1982;93:317–50.
[25] Lolck JE, Robiette AG, Brown LR, Hunt RH. Molecular Constants for the Interacting Upper States of the ν_1, ν_3, $2\nu_2$, $\nu_2 + \nu_4$, and $2\nu_4$ Bands in $^{12}CH_4$. Journal Molecular Spectroscopy 1982;92:229–45.
[26] Poussigue G, Pascaud E, Champion JP, Pierre G. Rotational analysis of vibrational polyads in tetrahedral molecules : Simultaneous analysis of the Pentad energy levels of $^{12}CH_4$. Journal Molecular Spectroscopy 1982;93:351–80.

[27] Hilico JC, Champion JP, Toumi S, Tyuterev V, Tashkun SA. New analysis of the Pentad system of methane and prediction of the Pentad-Pentad spectrum. Journal Molecular Spectroscopy 1994;168:455–76.
[28] Grigoriev I, Filippov N, Tonkov M, Champion J, Gabard T, Doucen RL. Line parameters and shapes of high clusters: R branch of the ν_3 band of CH_4 in He mixtures. Journal of Quantitative Spectroscopy and Radiative Transfer 2002;74:431–43.
[29] Féjard L, Champion J, Jouvard JM, Brown LR, Pine AS. The Intensities of Methane in the 3–5 μm Region Revisited. Journal of Molecular Spectroscopy 2000;201:83–94.
[30] Albert S, Bauerecker S, Boudon V, Brown LR, Champion JP, Loëte M, et al. Global analysis of the high resolution infrared spectrum of methane $^{12}CH_4$ in the region from 0 to 4800 cm^{-1}. Chemical Physics 2009;356:131–46.
[31] Daumont L, Nikitin A, Thomas X, Régalia L, der Heyden PV, Tyuterev V, et al. New assignments in the 2 μm transparency window of the $^{12}CH_4$ Octad band system. Journal of Quantitative Spectroscopy and Radiative Transfer 2013;116:101–9.
[32] Nikitin AV, Boudon V, Wenger C, Albert S, Brown LR, Bauerecker S, et al. High resolution spectroscopy and the first global analysis of the Tetradecad region of methane $^{12}CH_4$. Physical Chemistry Chemical Physics 2013;15:10071–93.
[33] Thiévin J, Georges R, Carles S, Benidar A, Rowe B, Champion JP. High-temperature emission spectroscopy of methane. Journal of Quantitative Spectroscopy and Radiative Transfer 2008;109:2027–36.
[34] Amyay B, Robert S, Herman M, Fayt A, Raghavendra B, Moudens A, et al. Vibration-rotation pattern in acetylene. II. Introduction of Coriolis coupling in the global model and analysis of emission spectra of hot acetylene around 3 μm. The Journal of Chemical Physics 2009;131:114301.
[35] Amyay B, Louviot M, Pirali O, Georges R, Vander Auwera J, Boudon V. Global analysis of the high temperature infrared emission spectrum of $^{12}CH_4$ in the dyad (ν_2/ν_4) region. The Journal of Chemical Physics 2016;144:24312.
[36] Louviot M, Suas-David N, Boudon V, Georges R, Rey M, Kassi S. Strong thermal nonequilibrium in hypersonic CO and CH_4 probed by CRDS. The Journal of Chemical Physics 2015;142(21):214305.
[37] Hargreaves RJ, Bernath PF, Bailey J, Dulick M. Empirical line lists and absorption cross sections for methane at high temperatures. The Astrophysical Journal 2015;813:12.
[38] Hargreaves RJ, Buzan E, Dulick M, Bernath PF. High-resolution absorption cross sections of C_2H_6 at elevated temperatures. Molecular Astrophysics 2015;1:20–5.
[39] Ba YA, Wenger C, Surleau R, Boudon V, Rotger M, Daumont L, et al. MeCaSDa and ECaSDa: Methane and ethene calculated spectroscopic databases for the virtual atomic and molecular data centre. Journal of Quantitative Spectroscopy and Radiative Transfer 2013;130:62–8.
[40] 2018. URL `http://vamdc.icb.cnrs.fr/PHP/methane.php`.
[41] Dubernet ML, Boudon V, Culhane J, Dimitrijevic M, Fazliev A, Joblin C, et al. Virtual atomic and molecular data centre. Journal of Quantitative Spectroscopy and Radiative Transfer 2010;111:2151–9.
[42] Dubernet ML, Antony BK, Ba YA, Babikov YL, Bartschat K, Boudon V, et al. The virtual atomic and molecular data centre (VAMDC) consortium. Journal of Physics B: Atomic, Molecular and Optical Physics 2016;49:074003.
[43] 2018. URL `http://portal.vamdc.org`.
[44] Gordon I, Rothman L, Hill C, Kochanov R, Tan Y, Bernath P, et al. The HITRAN2016 molecular spectroscopic database. Journal of Quantitative Spectroscopy and Radiative Transfer 2017;203:3–69.
[45] Rothman L, Gordon I, Barbe A, Benner D, Bernath P, Birk M, et al. The HITRAN 2008 molecular spectroscopic database. Journal of Quantitative Spectroscopy and Radiative Transfer 2009;110:533 –72.
[46] Carleer M. WSpectra: a Windows program to accurately measure the line intensities of high-resolution Fourier transform spectra. In: Russel J, Schäfer K, Lado-Bordowsky O, editors. Remote sensing of clouds and the atmosphere V, Proceedings of SPIE – The International Society for Optical Engineering; vol. 4168. 2001, p. 337.
[47] Champion JP. Développement complet de l'hamiltonien de vibration-rotation adapté à l'étude des interactions dans les molécules toupies sphériques. Application aux bandes ν_2 et ν_4 de $^{12}CH_4$. Canadian Journal of Physics 1977;55:1802–28.

[48] Loëte M. Developpement complet du moment dipolaire des molécules tétraédriques. Application aux bandes triplement dégénérées et à la diade ν_2 et ν_4. Canadian Journal of Physics 1983;61:1242–59.
[49] Champion JP, Loëte M, Pierre G. Spectroscopy of the Earth's atmosphere and interstellar medium. Academic Press, san Diego; 1992.
[50] Cheblal N, Loëte M, Boudon V. Development of the dipole moment and polarizability operators of octahedral molecules. Journal of Molecular Spectroscopy 1999;197:222–31.
[51] Nikitin A, Champion JP, Tyuterev VG. The MIRS computer package for modeling the rovibrational spectra of polyatomic molecules. Journal of Quantitative Spectroscopy and Radiative Transfer 2003;82:239–49.
[52] Boudon V, Champion JP, Gabard T, Loëte M, Michelot F, Pierre G, et al. Symmetry-adapted tensorial formalism to model rovibrational and rovibronic spectra of molecules pertaining to various point groups. Journal of Molecular Spectroscopy 2004;228:620–34.
[53] Wenger C, Champion JP. Spherical Top data system (STDS) software for the simulation of spherical top spectra. Journal of Quantitative Spectroscopy and Radiative Transfer 1998;59:471–80.
[54] Moret-Bailly J. Sur l'interprétation des spectres de vibration-rotation des molécules à symétrie tétraédrique ou octaédrique. Cah Phys 1961;15:237–316.
[55] Moret-Bailly J. Calculation of the frequencies of the lines in a threefold degenerate fundamental band of a spherical top molecule. Journal of Molecular Spectroscopy 1965;15:344–54.
[56] Zhilinskiĭ B. Reduction of rotational operators to standard form. Optics and Spectroscopy 1981;51:262–3.
[57] Champion JP, Pierre G, Michelot F, Moret-Bailly J. Composantes cubiques normales des tenseurs sphériques. Canadian Journal of Physics 1977;55:512–20.
[58] Rey M, Boudon V, Wenger C, Pierre G, Sartakov B. Orientation of O(3) and SU(2) $\otimes$ C_I representations in cubic point groups (O_h,T_d) for application to molecular spectroscopy. Journal Molecular Spectroscopy 2003;219:313–25.
[59] Stone AJ. Transformation between cartesian and spherical tensors. Mol Phys 1975;29.
[60] Boudon V, Pirali O, Roy P, Brubach JB, Manceron L, Auwera JV. The high-resolution far-infrared spectrum of methane at the SOLEIL synchrotron. Journal of Quantitative Spectroscopy and Radiative Transfer 2010;111:1117–29.
[61] Hilico JC, Barnov GS, Bronnikov DK, Gavrikov SA, Nikolav II, Rusanov VD, et al. High-Resolution spectroscopy of (Pentad-Dyad) and (Octad-Pentad) hot bands of Methane in a supersonic jet. Journal of Molecular Spectroscopy 1993;161:435–44.
[62] Bronnikov DK, Kalinin DV, Rusanov VD, Filimonov YG, Selivanov YG, Hilico JC. Spectroscopy and non-equilibrium distribution of vibrationally excited methane in a supersonic jet. Journal of Quantitative Spectroscopy and Radiative Transfer 1998;60:1053–68.
[63] Abe M, Iwakuni K, Okubo S, Sasada H. Accurate transition frequency list of the ?3 band of methane from sub-Doppler resolution comb-referenced spectroscopy. Journal of the Optical Society of America B 2013;30:1027.
[64] Bray C, Cuisset A, Hindle F, Mouret G, Bocquet R, Boudon V. Spectral lines of methane measured up to 2.6 THz at sub-MHz accuracy with a CW-THz photomixing spectrometer: Line positions of rotational transitions induced by centrifugal distortion. Journal of Quantitative Spectroscopy and Radiative Transfer 2017;203:349–54.
[65] Wenger C, Boudon V, Rotger M, Sanzharov M, Champion JP. XTDS and SPVIEW: Graphical tools for the analysis and simulation of high-resolution molecular spectra. Journal of Molecular Spectroscopy 2008;251:102–13.
[66] Bermejo D, Santos J, Cancio P. High-resolution q-cw SRS Spectrum of $^{12}CH_4$ in the Region of the Level Crossing between ν_1 and $\nu_2 + \nu_4$. Journal of Molecular Spectroscopy 1992;156:15–21.
[67] Rey M, Nikitin AV, Babikov YL, Tyuterev VG. TheoReTS – An information system for theoretical spectra based on variational predictions from molecular potential energy and dipole moment surfaces. Journal of Molecular Spectroscopy 2016;327:138–58.
[68] Tennyson J, Yurchenko SN, Al-Refaie AF, et al. . The ExoMol database: Molecular line lists for exoplanet and other hot atmospheres. Journal of Molecular Spectroscopy 2016;327:73–94.
[69] Jacquinet-Husson N, Armante R, Scott N, Chédin A, Crépeau L, Boutammine C, et al. The 2015 edition of the GEISA spectroscopic database. Journal of Molecular Spectroscopy 2016;327:31–72.

Table 1: Experimental conditions used to record the six emission spectra of methane. The numbers between parentheses are the uncertainties, in the units of the last digits quoted.

No.	I	Q_{CH_4}	P	N_{scans}	Res.	T
	A	l_n/min	Pa		cm^{-1}	K
1	20	3	6.93	2500	0.012	620 (5)
2	50	3	7.20	1200	0.012	918 (5)
3	80	3	8.12	2000	0.008	1404 (10)
4	100	3	8.80	2000	0.020	1479 (12)
5	130	3	10.66	2000	0.020	1532 (20)
6	130	1.5	9.33	1800	0.020	1715 (25)

I : Electric current
Q_{CH_4}: Mass flow rate of methane (normal liter per minute)
P: Pressure of the vacuum chamber
N_{scans}: Number of interferograms averaged
Res.: Spectral resolution
T: Gas temperature

Table 2: Number of parameters in the effective Hamiltonian for the different orders. The numbers between parentheses indicate the number of fitted parameters in each case; non-fitted parameters were fixed to zero. The total number of fitted line positions was 39614 (34811 in Ref. [35]).

Order	$\widetilde{H}^{\langle\text{Tetradecad}\rangle}_{\{\text{GS}\}}$		$\widetilde{H}^{\langle\text{Tetradecad}\rangle}_{\{\text{Dyad}\}}$		$\widetilde{H}^{\langle\text{Tetradecad}\rangle}_{\{\text{Pentad}\}}$		$\widetilde{H}^{\langle\text{Tetradecad}\rangle}_{\{\text{Octad}\}}$		$\widetilde{H}^{\langle\text{Tetradecad}\rangle}_{\{\text{Tetradecad}\}}$		$\widetilde{H}^{\langle\text{Tetradecad}\rangle}$	
0	1	(1)	2	(2)	2	(2)	0	(0)	0	(0)	5	(5)
1	0	(0)	2	(2)	5	(5)	0	(0)	0	(0)	7	(7)
2	2	(2)	6	(6)	21	(21)	13	(12)	7	(7)	49	(48)
3	0	(0)	6	(6)	35	(35)	57	(56)	36	(30)	134	(127)
4	3	(3)	13	(13)	71	(71)	183	(181)	219	(113)	489	(381)
5	0	(0)	11	(11)	94	(94)	343	(331)	672	(126)	1120	(562)
6	4	(4)	22	(22)	154	(150)	0	(0)	0	(0)	180	(176)
Total	10	(10)	62	(62)	382	(378)	596	(580)	934	(276)	1984	(1306)
Ref.[35]	10	(10)	62	(62)	228	(218)	596	(539)	934	(267)	1830	(1096)

Table 3: Summary of vibration-rotation transitions of methane $^{12}CH_4$ included in the global analysis.

Transition $P_{n'} - P_{n"}$	Region cm^{-1}	# data	$J"_{min}$	$J"_{max}$	d_{RMS} 10^{-3} cm^{-1}	Ref.
$P_0 - P_0$	0.008 - 2506.481	135	2	19	102.625 (kHz for Q branch) 0.143 (R branch)	[32],[60],[64]
$P_1 - P_0$	1023.275 - 1778.830	2224	0	30	2.832	[32],[35]
$P_2 - P_0$	2207.366 - 3274.188	5876	0	30	3.946	[32],[63],This work
$P_3 - P_0$	3518.877 - 4746.620	7907	0	18	5.948	[32]
$P_4 - P_0$	4885.723 - 6204.613	3009	0	14	23.225	[32]
$P_1 - P_1$	13.402 - 2532.357	124	1	14	148.717 (kHz for Q branch) 0.180 (R branch)	[32],[60],[64]
$P_2 - P_1$	1100.443 - 1930.376	5272	0	29	4.523	[32],[35]
$P_3 - P_1$	2334.157 - 3298.380	4932	0	27	8.392	[32],This work
$P_2 - P_2$	6.895 - 17.391	16	4	12	178.142 (kHz for Q branch)	[32]
$P_3 - P_2$	1102.505 - 1426.872	6454	0	28	6.579	[32],[35]
$P_4 - P_2$	2822.352 - 3175.063	1525	1	20	11.759	This work
$P_4 - P_3$	1129.633 - 1382.236	2140	1	21	6.518	[35]

Table 4: Fit statistics for the line intensities calculation of methane $^{12}CH_4$. Comparisons with the previously published fits in the literature are given between parenthesis for each band.

Bands	# fit. lines	J_{max}	# parameters	d_{RMS} (Litt.) %	St.Dev. (Litt.)	Ref.
$P_0 - P_0$	92	18	3	8.51 (8.52)	1.49 (1.47)	[60]
$P_1 - P_1$	96	14	3	8.85 (8.74)	1.36 (1.31)	[60]
$P_1 - P_0$	1189	22	27	3.23 (3.38)	1.33 (1.42)	[30]
$P_2 - P_1$	881	12	27	4.55 (5.19)	1.40 (1.58)	[30]
$P_2 - P_0$	2534	21	28	5.16 (3.01)	1.78 (1.03)	[30]
$P_3 - P_0$	3153	20	95	12.66 (8.20)	11.74 (8.11)	[30]
$P_4 - P_0$	1451	14	40	14.42 (14.18)	13.99 (13.86)	[32]

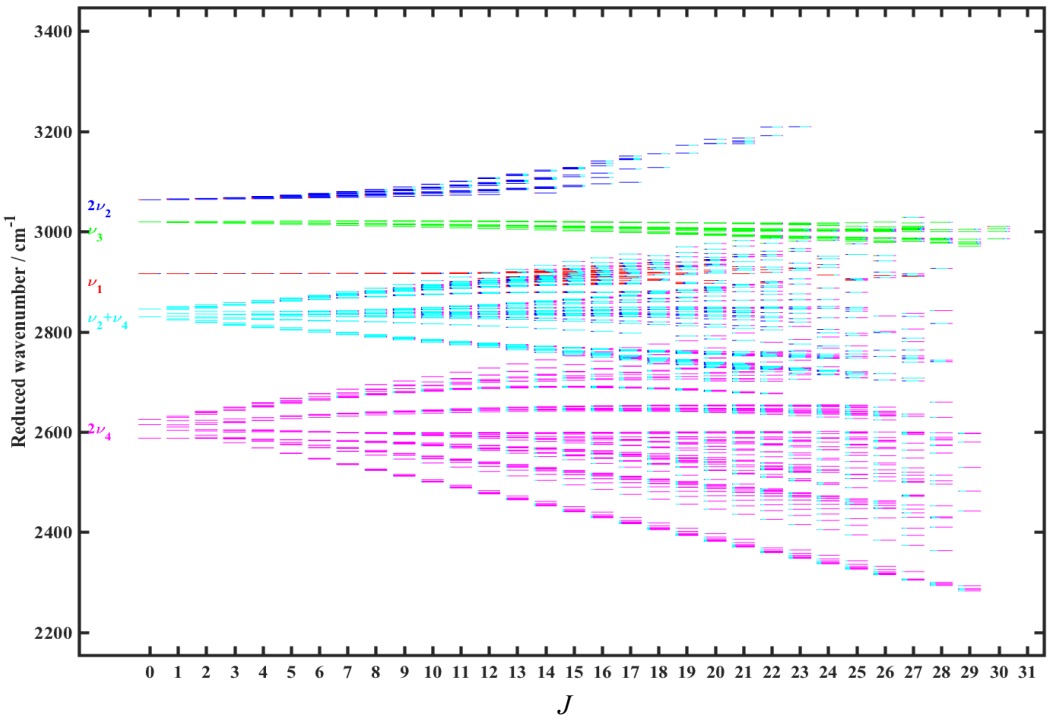

Figure 1: The reduced energy levels of $^{12}CH_4$ in the Pentad region up to $J_{max} = 30$. Vibrational states are assigned using the conventional normal modes ν_k with $(k = 1, 2, 3$ and $4)$. Different colors are used for each vibrational state to highlight the weavefunction mixings.

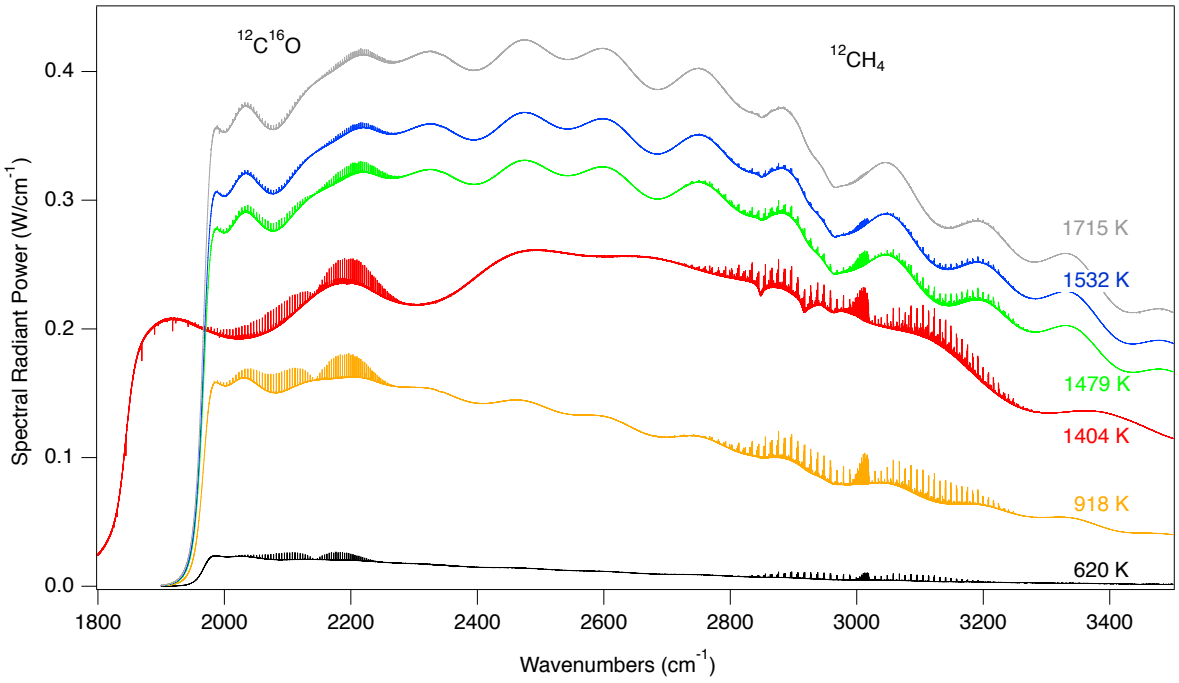

Figure 2: High-temperature (from 620 to 1715 K) high-resolution emission spectra of methane in the Pentad region. The 1–0 CO emission band is used to measure the rotational temperature. The emission continuum is produced by the graphite walls of the high enthalpy source. An intensity scaling factor of 0.7 was applied in the case of the emission spectrum at 1404 K.

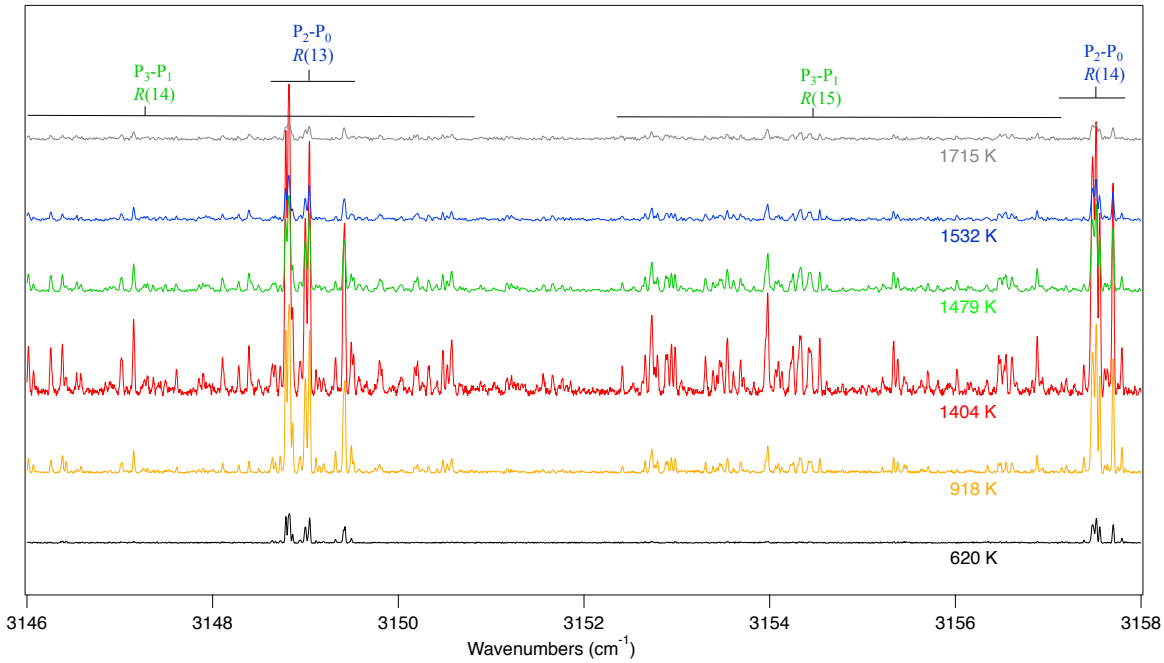

Figure 3: Zoom in on a small portion of the R branch between 3146-3158 cm^{-1} of the high temperature emission spectra of methane. The baseline observed in each spectrum (see Figure 2) was removed and the spectra are shifted vertically for clarity.

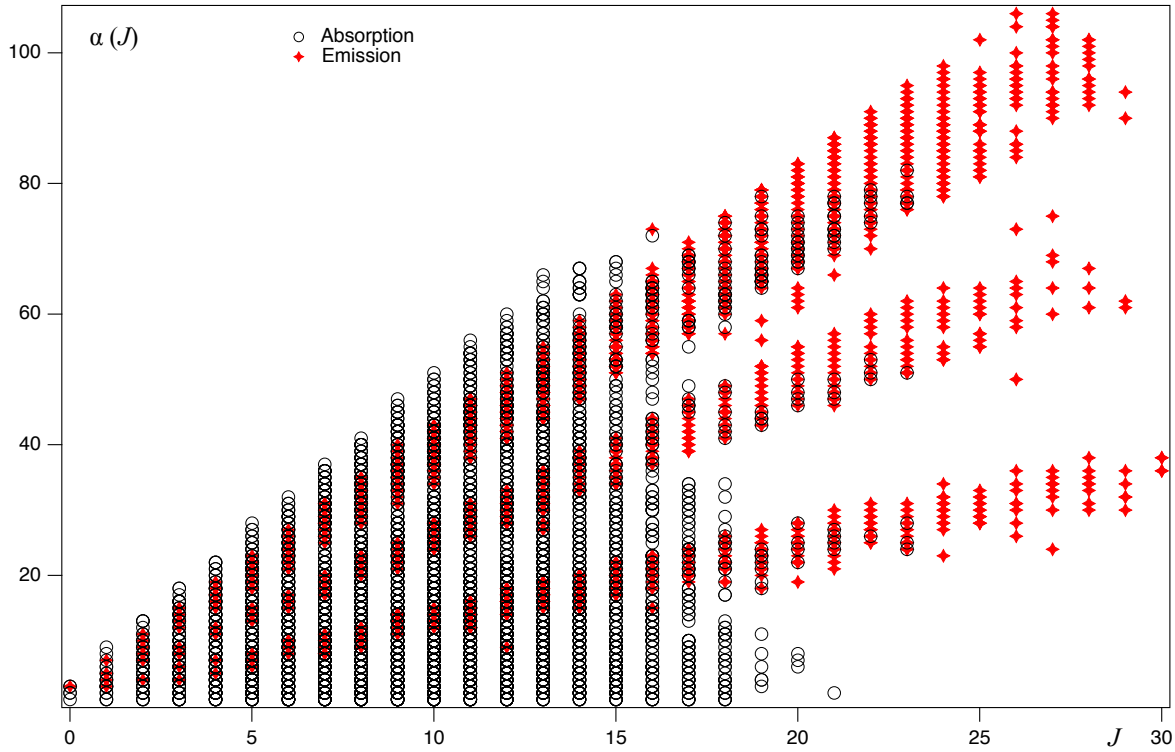

Figure 4: Comparison between previously observed transitions in the Pentad system and the present analysis. The ranking number α corresponding to observed levels is plotted in function of the rotational quantum number J.

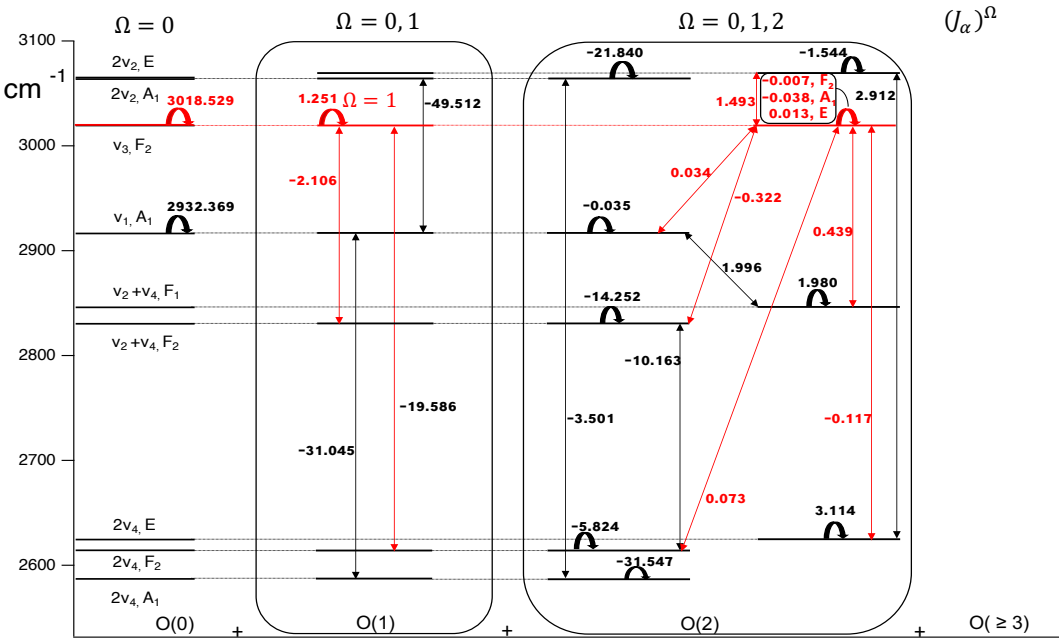

Figure 5: The Pentad interacting system up to the order 2 of the effective Hamiltonian development. The couplings between sub-states are highlighted using arrows. The red color is used for couplings involving the ν_3 state. The order of magnitude of each coupling term is given in cm^{-1} as resulting from the present global fit. The rotational dependency of illustrated couplings is indicated in the top of the Figure.

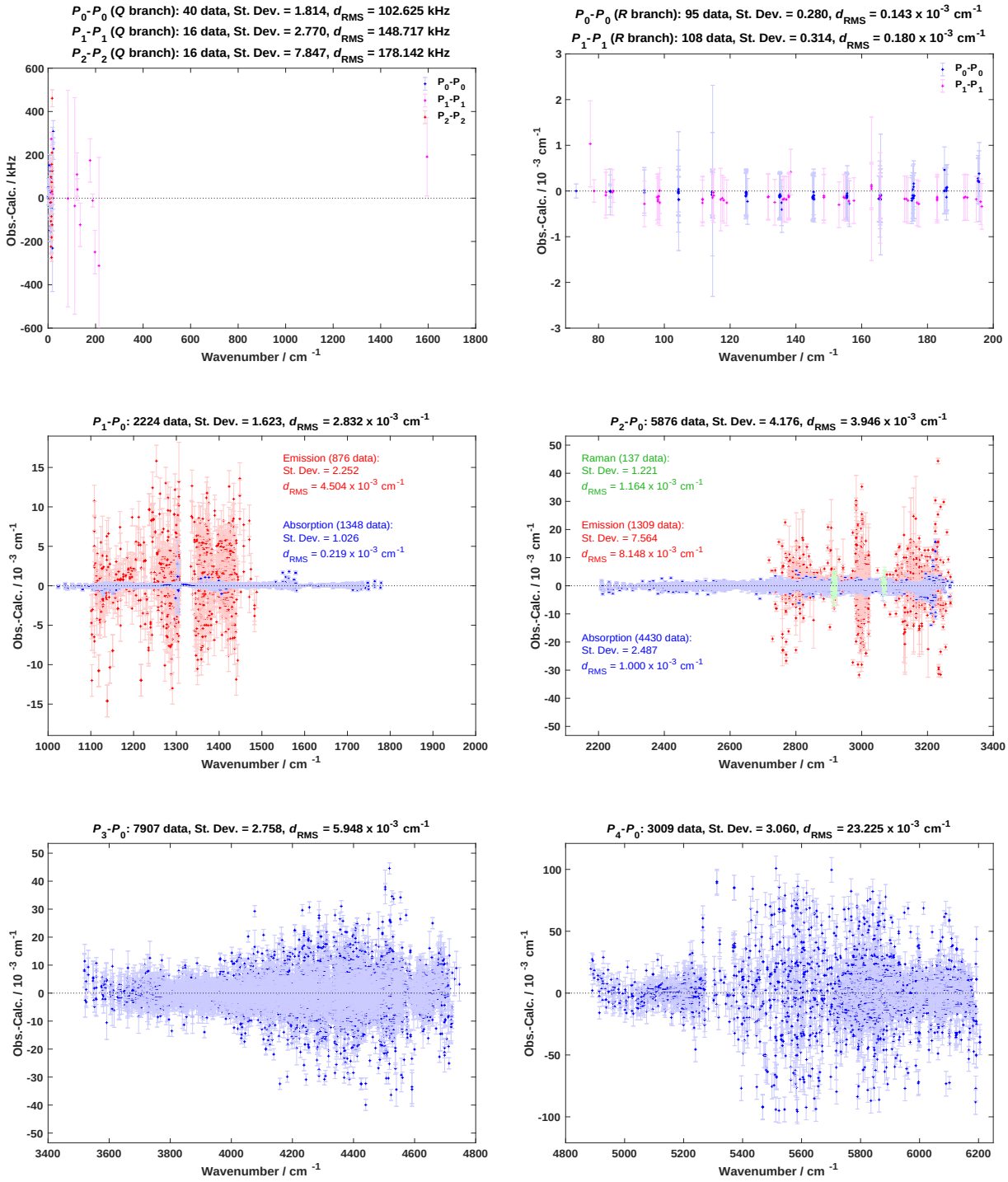

Figure 6: Fit residuals (Obs.- Calc.) for both rotational transitions ($P_x - P_x$) and the cold bands. Emission data are highlighted in red while absorption data previously assigned or newly added from the literature are illustrated in blue. Few Raman data belonging to ($P_2 - P_0$) are also highlighted in green. For each band, the total number of transitions and their corresponding standard deviation and (RMS) are given. Error bars correspond to the weight assigned to each transition in the fit procedure.

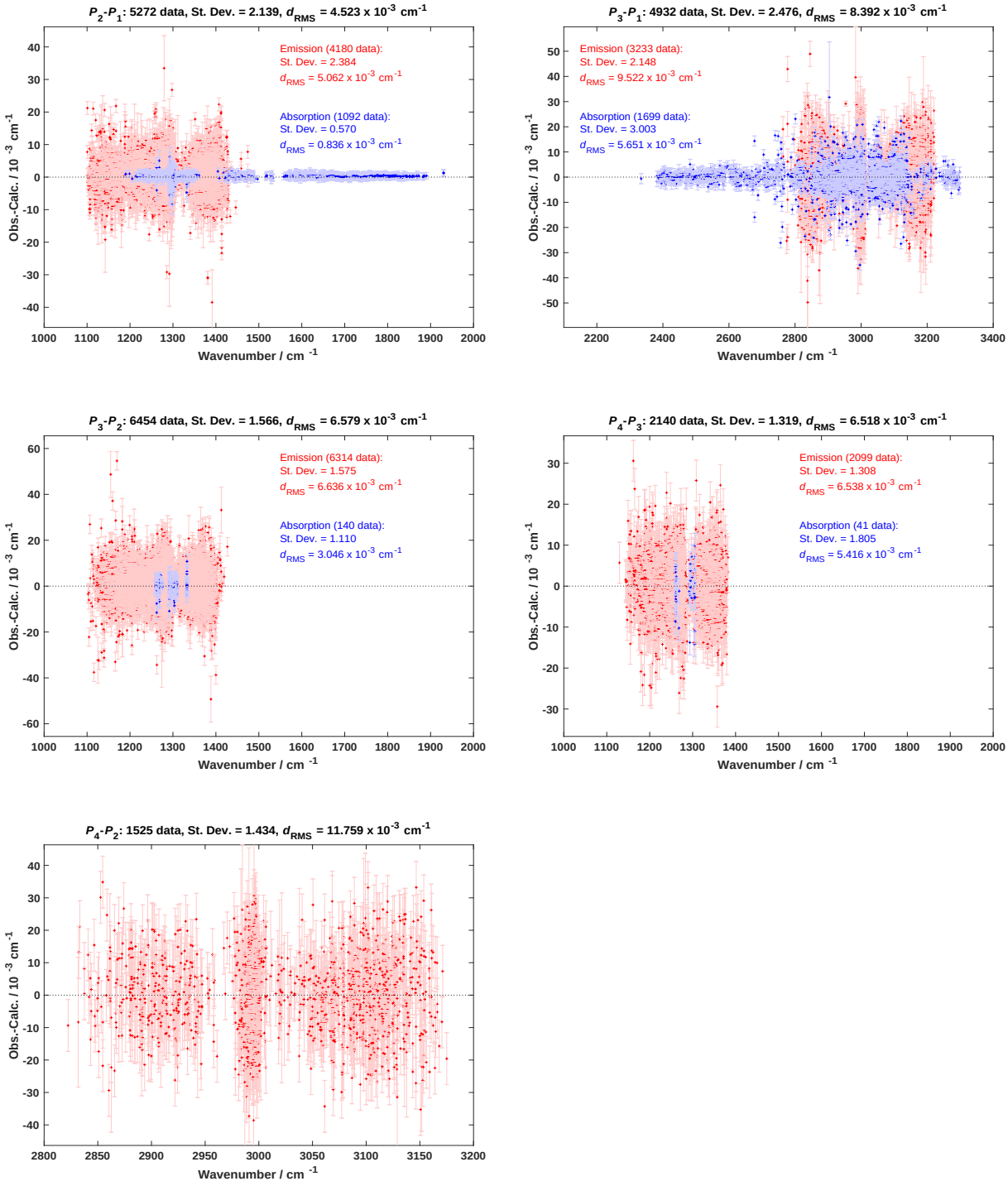

Figure 7: Fit residuals (Obs.- Calc.) for line positions corresponding to assigned hot bands. Emission data are highlighted in red while absorption data previously assigned or newly added from the literature are illustrated in blue. For each band, the total number of transitions and their corresponding standard deviation and RMS are given. Error bars correspond to the weight assigned to each transition in the fit procedure.

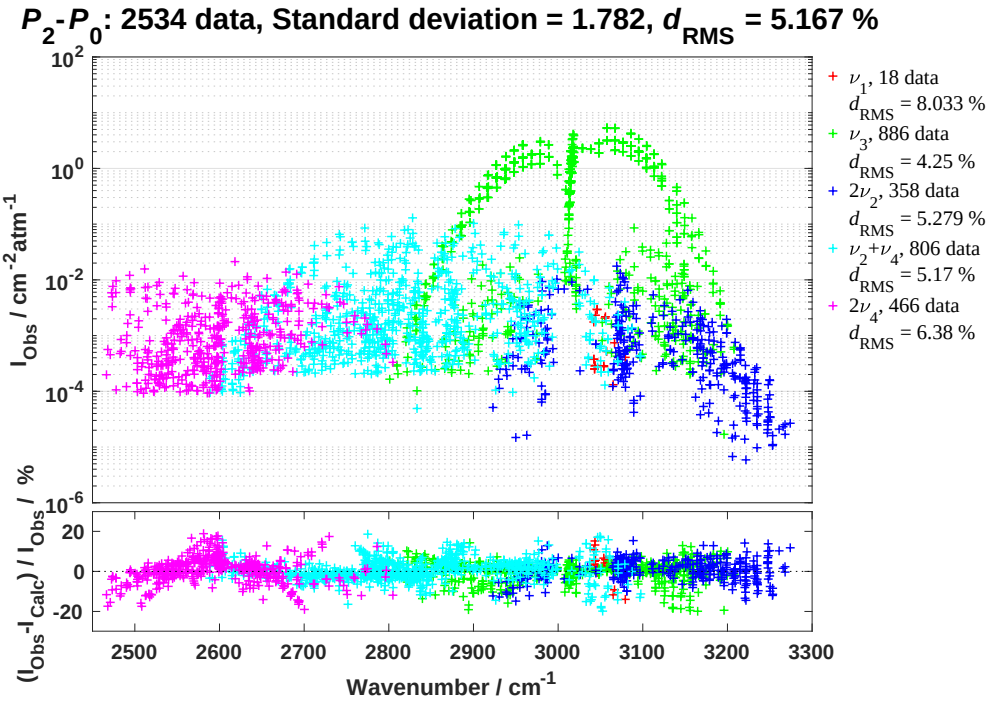

Figure 8: Fit residuals for observed line intensities at 296 K (I_{obs}) in the Pentad−GS system of $^{12}CH_4$. Absolute line intensities are plotted in the top part of the Figure using a logarithmic scale. Different sub-bands are distinguished using different colors. Intensity residuals are given in % at the bottom using the same color code.

Figure 9: Comparison between the observed spectrum of $^{12}CH_4$ at 1404 K (red) and the calculated spectrum (grey) in the spectral region 2600-3300 cm^{-1}. The contribution of the cold band (blue) and related hot-bands (green and cyan) are highlighted separately in the bottom of each sub-figure. Also a comparison with the TheoReTS calculated database (brown curve) is given for both low and high J transitions in the bottom of each sub-figure.

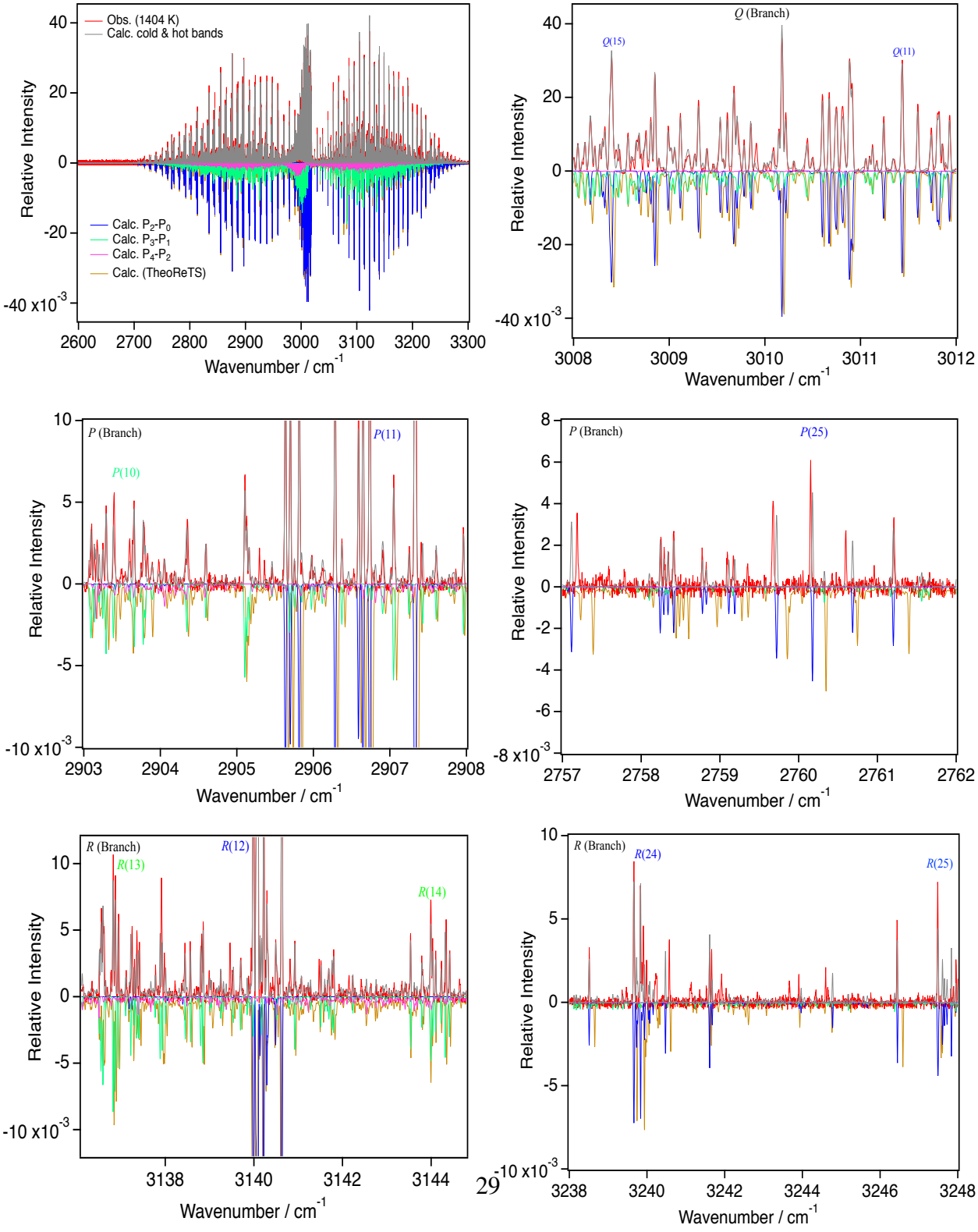

Figure 10: Low resolution (1 cm^{-1}) calculated cross-sections of $^{12}CH_4$ at 296 K in the spectral region between 0 and 6500 cm^{-1} from MeCaSDa (red), ExoMol (green) and TheoReTS (from the 500 K line liste, blue) line lists, respectively. The insert shows a zoom around the ν_3 band center.